This article has been accepted for inclusion in a future issue of this journal. Content is final as presented, with the exception of pagination.

Modeste Bodehou, Khaldoun Al Khalifeh, Shambhu Nath Jha, and Christophe Craeye

Direct Numerical Inversion Methods for the Design of Surface Wave-Based Metasurface Antennas

Fundamentals, realizations, and perspectives.

xxxxx

A recent synthesis paradigm for tailoring the far-field radiation of leaky wave (LW) radiating metasurface (MTS) antennas is reviewed and experimentally validated. The considered antennas are realized with electrically small patches printed on a planar grounded dielectric slab. The patch layer is modeled as an impedance sheet whose spatial variation is initially designed to provide the desired LW effect from a prespecified surface wave (SW) excitation.

The synthesis method is based on the direct numerical solution of the surface integral equation enforcing the sheet impedance boundary condition (IBC), the latter of which accurately describes the wave–MTS interaction in the homogenized limit. The class of synthesizable anisotropic impedance profiles is very general and enables the generation of shaped beams with control of the amplitude, phase, and polarization. The method has been extended toward the generation of multiple-beam and multifunctional operation. The obtained designs are translated into the distribution of small patches based on an efficient periodic method of moments (MOM) solver. Numerical and experimental validations are provided, showing the effectiveness of the method. Short- to medium-term perspectives are also summarized.

Digital Object Identifier 10.1109/MAP.2022.3169344
Date of current version: 7 June 2022

INTRODUCTION

Shaping the radiation pattern of an antenna is an appealing functionality in many applications, including radar [1], space [2], and mobile communications [3]. In addition, the global trend in wireless systems development is toward compactness. This calls for low-profile electromagnetic (EM) structures with extreme beam-shaping capabilities, i.e., with a good control on the amplitude, phase, and polarization of the radiation pattern. In this sense, recent developments on MTS technology are very promising [4]–[7].

MTSs are thin surfaces composed of electrically small elements arranged so as to exhibit unusual macroscopic properties in a given frequency band [8]. At the wavelength of operation, those surfaces can be accurately described as a modulated electric sheet impedance, which can possibly be cascaded to achieve more elaborate EM properties: generalized sheet transition conditions [9]. MTSs can be used to control the transmission of a pre-established wave so as to arbitrarily transform this wave on the other side of the surface [10]–[12]. They have also found applications in manipulating reflected waves [13]. A reflecting-beam MTS can be used as an antenna [14] or to control the propagation channel in the context of mobile communications [15].

When dealing with MTS antennas, one technology is of specific interest due to its particularly low-profile shape: LW MTS antennas [4]. Indeed, contrary to MTSs operating in transmission or reflection, which require a noncoplanar feeder, LW MTS structures are fed with an integrated SW launcher. The MTS is designed to progressively transform the SW provided by the feed into properly radiated LWs. Even if the theoretical intuition behind this technology goes back to the work of Oliner and Hessel [16] several decades ago, many new developments in MTS engineering were necessary to reach practical implementations.

The first antenna design based on this technology was provided by the group of Sievenpiper [17], who proposed an holographic technique in which the MTS characteristics are derived from the interference between the desired beam and SW field. Along the same lines, Patel and Grbic [18] addressed the synthesis of 1D sinusoidally modulated MTS antennas. Progress in this technology has rapidly taken place over the last decade, in particular with the contributions of Maci's group, which has successively introduced amplitude-based synthesis [19], aperture field synthesis [20], multibeam [21], wideband operation [22], and so on.

In those works, the anisotropic MTS modulation is assumed to be locally sinusoidal; i.e., the period of the sinusoid as well as its amplitude can be smoothly modulated. This allows one to describe the local MTS modulation as a sinusoid, consequently supporting an infinite set of Floquet modes. The propagation constant of each mode and attenuation factor of the SW as well as the energy transfer toward the radiating and evanescent Floquet modes can be extracted locally using a proposed flat optics theory [23]. The latter models the MTS as a sheet impedance that linearly relates the averaged electric field and homogenized electric current at the level of the metallization.

Very recently, another synthesis approach was proposed and successfully applied for shaped-beam [5], [6], multibeam [6], [24], and multiband operation [25]. Contrary to the previous techniques, this approach does not require the determination of the attenuation factor or propagation constant, as are traditionally established when designing LW antennas. Moreover, no locally sinusoidal modulation is assumed; i.e., the MTS's surface impedance can be arbitrarily modulated. That is made possible because this synthesis method is directly based on the surface integral equation, as is traditionally the case for an EM analysis with MOM [26].

Another synthesis method relying on the surface integral equation was also proposed very recently [27]; so far, it has been demonstrated with MTSs that are infinitely periodic in one direction in a reflectarray-type configuration. The algorithm presented here can be used to generate arbitrarily shaped 3D patterns and multiple-shaped-beam, multiband [25] patterns from a single ultralow profile structure including the feed.

Let us consider an MTS antenna modeled as an impedance sheet lying on a infinitely extended grounded slab (see Figure 1). It appears that it is possible to numerically compute the sheet impedance modulation from the desired aperture current: this constitutes the basic block of the direct numerical inversion method, the key point being the explicit enforcement of the EM boundary conditions at the level of the sheet impedance. The goals of this article are to review this novel approach in a more intuitive way, provide a new numerical and physical perspective on this approach, and showcase the experimental validation.

FROM NUMERICAL ANALYSIS TO DIRECT INVERSION

As a first step, the analysis of MTSs with MOM is reviewed; it is used to understand the solution of the inverse problem. We consider an MTS represented as an impedance sheet distribution on a grounded slab (see Figure 1). The sheet impedance $\underline{\underline{\mathbf{Z}}}_S$ (assumed to be capacitive in this article) imposes the ratio between the total electric field and surface current $\underline{\mathbf{J}}$ at the MTS. The surface integral equation to be solved is, therefore, given by

$$\hat{\mathbf{z}} \times \left[\int\!\!\int_{S'} \underline{\underline{\mathbf{G}}}^{EJ}(\boldsymbol{\rho}, \boldsymbol{\rho}') \underline{\mathbf{J}}(\boldsymbol{\rho}')\, dS' - \underline{\underline{\mathbf{Z}}}_S(\boldsymbol{\rho})\, \underline{\mathbf{J}}(\boldsymbol{\rho}) \right] = -\hat{\mathbf{z}} \times \underline{\mathbf{E}}_i, \quad (1)$$

where $\hat{\mathbf{z}}$ is the unit vector normal to the surface, $\underline{\underline{\mathbf{G}}}^{EJ}$ is the spatial Green's function of the grounded slab, and $\underline{\mathbf{E}}_i$ is the antenna excitation. Finally, the source and observation points at the surface are $\boldsymbol{\rho}'$ and $\boldsymbol{\rho}$, respectively, and the integration is carried out over the MTS aperture [29]. When analyzing the MTS, the current $\underline{\mathbf{J}}$ is unknown and is expanded into a set of basis functions $\underline{\mathbf{F}}_n$; i.e.,

$$\underline{\mathbf{J}} \approx \sum_{n=1}^{N} i_n \underline{\mathbf{F}}_n, \quad (2)$$

where the coefficients of expansion i_n are determined after forcing the integral equation with a set of testing functions. The latter are usually the same as those used as basis functions (Galerkin testing).

The integral equation is, therefore, transformed into an algebraic linear system of equations, which can be represented graphically as shown in Figure 2. In that figure, $\mathbf{Z}_G$ is the so-called substrate matrix and represents the fields radiated by each basis function in the presence of the substrate, tested by each testing function; each row stands for the use of a different testing function. Details regarding the calculation of the substrate matrix $\mathbf{Z}_G$ with the slab Green's function can be found in

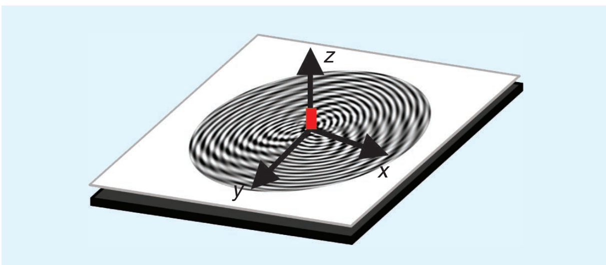

FIGURE 1. An LW MTS antenna.

[29]. $\mathbf{Z}_{IBC}$ is the IBC matrix, translating the sheet IBC. More precisely, each element of $\mathbf{Z}_{IBC}$ is the field associated with each basis function current, given the presence of the sheet impedance (i.e., the product between the basis function and sheet impedance), tested by a given testing function. Each element of $\mathbf{Z}_{IBC}$ is given by

$$Z_{IBC}(n,n') = \int\int_S \underline{\mathbf{F}}_n(\boldsymbol{\rho})\,\underline{\underline{\mathbf{Z}}}_S(\boldsymbol{\rho})\,\underline{\mathbf{F}}_{n'}(\boldsymbol{\rho})dS, \qquad (3)$$

where the indices n' and n represent a given scalar basis/testing function, respectively, and the integration is carried out over the MTS [29].

Now, assuming that the sheet impedance is modulated around an average $\underline{\underline{Z}}_0$, the modulation can be expanded into a set of basis functions [5], although it is presented here with a somewhat generalized notation:

$$\underline{\underline{\mathbf{Z}}}_S = \underline{\underline{Z}}_0 + \underline{\underline{\mathbf{P}}} \approx \underline{\underline{Z}}_0 + \sum_{k=1}^{K} c_k\,\underline{\underline{\mathbf{F}}}_k, \qquad (4)$$

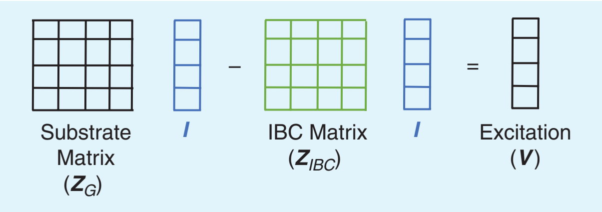

FIGURE 2. The system of equations to be solved for the analysis problem.

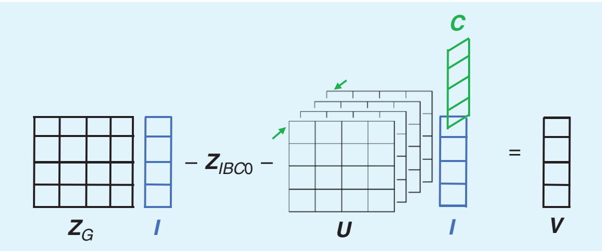

FIGURE 3. The system of equations to be solved for the analysis problem after the discretization of the surface impedance.

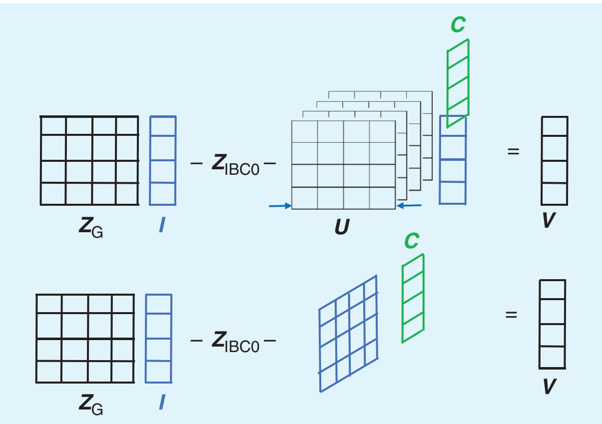

FIGURE 4. The system of equations to be solved for the inverse problem.

where c_k represents the coefficients of expansion, $\underline{\underline{\mathbf{P}}}$ is the anisotropic modulation, and $\underline{\underline{\mathbf{F}}}_k$ represents the tensorial basis functions used for the sheet impedance modulation expansion. Each element of the IBC matrix can, therefore, be obtained as

$$Z_{IBC}(n,n') = Z_{IBC0}(n,n') + \sum_{k=1}^{K} c_k \int\int_S \underline{\mathbf{F}}_n\,\underline{\underline{\mathbf{F}}}_k\,\underline{\mathbf{F}}_{n'}dS, \qquad (5)$$

which can be written in matrix form as

$$\mathbf{Z}_{IBC} = \mathbf{Z}_{IBC0} + \mathbf{U}\cdot C, \qquad (6)$$

where $\mathbf{Z}_{IBC0}$ is the IBC matrix calculated with the average impedance $\underline{\underline{Z}}_0$, and $\mathbf{U}$ is a 3D matrix of size (N, N, K), whose elements are given by $U(n,n',k) = \int\int_S \underline{\mathbf{F}}_n\,\underline{\underline{\mathbf{F}}}_k\,\underline{\mathbf{F}}_{n'}dS$. Finally, C is a vector containing the coefficients c_k of the surface impedance expansion. The matrix–vector product between $\mathbf{U}$ and C is carried out along the indices k. That means that the representation of Figure 2 is equivalent to the one in Figure 3. From there, the solution of the inverse problem, i.e., the determination of the c_k coefficients in (4), becomes intuitive. Indeed, assuming that the current is known, the impedance can be retrieved from the current, as illustrated in Figure 4. The mathematical details of the method can be found in [5].

FROM THE INVERSE PROBLEM SOLUTION TO THE SYNTHESIS ALGORITHM

Up to now, we have explained how to compute the surface impedance consistent with a desired current distribution. In practice, however, the desired current distribution is not known. What is known is the desired radiation pattern, which can be translated into the visible spectrum of the desired current (see Appendix B of [5]). Decomposing the aperture fields into plane waves with the wave vector (k_x, k_y, k_z), the visible spectrum is the part of the spectrum for which $\sqrt{k_x^2+k_y^2} < k_0$, with $k_0 = 2\pi/\lambda$ being the free-space wavenumber. The fundamental question is, therefore, what about the invisible spectrum of currents that produces the evanescent fields?

When designing arbitrarily shaped beams, those currents cannot be inferred from the far fields. This issue has been studied in [31] for the design of reflectarrays satisfying a user-defined geometry. The physical principles of the MTS antenna are based on an SW transformed into a LW; the invisible part of the spectrum is quite substantial, and an initial assumption will consist of obtaining that part of the spectrum from the unmodulated reactance, i.e., based on the analysis of an MTS characterized by the constant sheet impedance $\underline{\underline{Z}}_0$.

The objective current is, then, obtained as the sum of the estimate of the invisible current and the desired visible current. Note that the visible current should be rescaled with respect to the desired radiated power. The latter is obtained from the total power delivered by the feed in the absence of modulation. This power can be calculated with one of the two algorithms proposed in [28]. Based on the objective current, the impedance modulation can be derived as explained in the "From Numerical Analysis to Direct Inversion" section while algebraically imposing the surface impedance tensor to be antihermitian (i.e., without losses).

It is worth mentioning that the grounded substrate has been assumed to be infinite so as to enable the use of Green's functions for layered media. Since, in practice, the grounded slab is not infinite, one should pay attention to the possible diffraction or reflection effects at the substrate rim. The limitation of those effects requires a high conversion efficiency, i.e., a high ratio between the radiated power (assuming an infinite slab) and the power delivered by the feed. Therefore, once the impedance modulation has been computed, the conversion efficiency should be checked. If the conversion efficiency is high enough ($> 80\%$), the prediction of the infinite slab model is relatively accurate, as experimentally demonstrated in [4] and [28].

In case the conversion efficiency is not high enough, two corrections can be envisaged. The first one corresponds to increasing the ratio between the visible and invisible currents (i.e., increasing the desired radiated power). The second correction consists of increasing (optimizing) the modulation depth, bearing in mind that it may slowly degrade the fidelity to the desired pattern as well as reduce the aperture efficiency since the surface wave will leak sooner. Note that, at this step, a more accurate estimate of the invisible current spectrum can be obtained based on the one computed after numerically analyzing the previously designed impedance surface. This new estimation of the invisible current can be used in a next iteration, as done in [24]. Optimization of the overall efficiency is a complex issue that deserves further attention and may require a properly designed feeder [6]. The algorithm is summarized in Figure 5.

Since the synthesis method leads to a linear system of equations to be solved, the design of an MTS radiating multiple beams with multiple feeds and, more generally, multifunctional operation is possible by overconstraining the system of equations or by imposing specific constraints on the impedance profile. Indeed, one can stack the systems of equations corresponding to each beam/feed and solve the overall system in the least-squares sense [24]. Of course, since more conditions are imposed with, essentially, the same degrees of freedom on the surface, one may expect some degradation of the fidelity with which beams are produced.

SURFACE IMPEDANCE IMPLEMENTATION

Once the surface impedance has been synthesized, it is necessary to implement it with electrically small patches to obtain the physical structure of the MTS. To do so, we discretized the antenna aperture using a rectangular grid with a unit-cell size of $a = \lambda/7$. Considering that the impedance variation is very slow at the unit-cell scale, it can be assumed that the scatterers implementing the surface impedance are immersed in an infinitely periodic environment (a local periodicity assumption [32], [19]). The extraction of the surface impedance tensor is based on in-house periodic MOM software. The efficiency and accuracy of that in-house software is ensured through the extraction of periodic singularities in an average-permittivity homogeneous medium. The latter is efficiently computed through a line-by-line approach, which is described in [37]. The remainder of Green's function is tabulated in 2D for the further use of convolution in the space domain with the basis and testing functions.

The coffee bean patch proposed in [19] (see Figure 6) has been adopted for the surface impedance implementation. Varying the diameter b of the patch and its orientation (ψ) allows one to construct a database of the sheet impedance tensor as a function of b and ψ [19]. The sheet impedance database is built using a procedure similar to the one described in [32]. The supported SW mode k_{sw} (the eigenmode) is computed by looking for possible nonzero solutions to the MOM system of equations in the absence of excitation. This amounts to looking in the Brillouin region for the mode ($k_\rho = \sqrt{k_x^2 + k_y^2}$) that nulls the determinant of the periodic MOM matrix; i.e.,

$$\det(\mathbf{Z}_{\mathrm{MOM}}(\boldsymbol{k}_{sw})) = 0. \tag{7}$$

This process is accelerated by interpolating the periodic MOM matrix versus k_ρ. Once the eigenmode k_{sw} has been obtained, the sheet impedance tensor is extracted following the method described in [34]. This process is carried out over a continuum of coffee bean patch orientations and diameters, resulting in the impedance tensor map represented in Figure 6(b)–(d). From that, the implementation of the surface impedance in each unit-cell center is obtained after minimizing the following cost function:

$$\sqrt{(X_S^{\rho\rho} - X_{TM})^2 + (X_S^{\rho\phi} - X_{TMTE})^2 + \beta(X_S^{\phi\phi} - X_{TE})^2}, \tag{8}$$

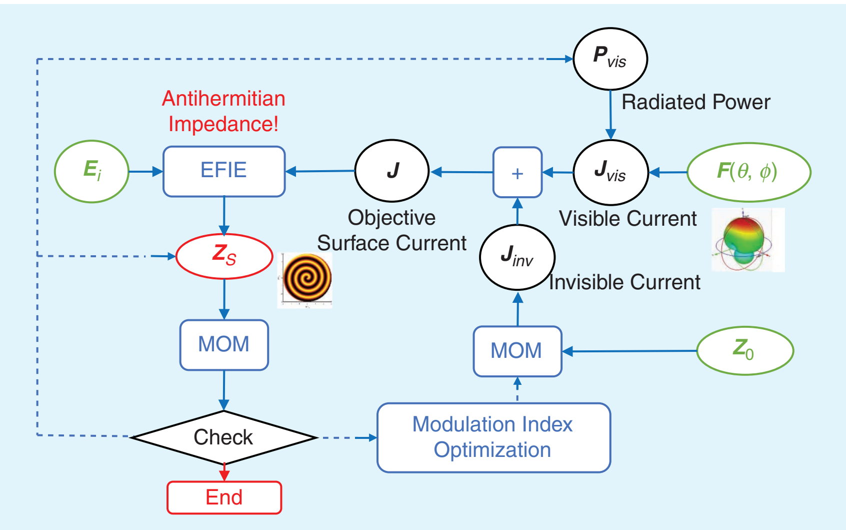

FIGURE 5. The synthesis algorithm. The green quantities are known.

where X_{TM}, X_{TE}, and X_{TMTE} are, respectively, the transverse magnetic (*TM*), transverse electric (*TE*), and *TMTE* realizable impedance components in the database. β is a coefficient used to weight the relative importance of the *TE* component with respect to the other components. Since the mode supported by those antennas is quasi-*TM*, one can introduce more tolerance on the *TE* component to better implement the other components. Here, we have used $\beta = 0.1$. The implementation process results in a map giving the diameter and orientation of the coffee bean patch in each unit cell.

RESULTS

This section provides four validations of the numerical inversion method. The operating frequency is fixed to $f = 24$ GHz. The substrate is assumed to be lossless, with relative permittivity $\epsilon_r = 3.66$ and thickness $d_{\text{slab}} = 1.524$ mm. The average reactance $(\underline{\underline{Z}}_0 = j\underline{\underline{X}}_0)$ is chosen as $X_0^{\rho\rho} = X_0^{\phi\phi} = -772\ \Omega$ so as to be implementable with the coffee bean patches. The anisotropic MTS impedance is capacitive and modulated as [5]

$$\begin{aligned} Z_S^{\rho\rho}(\rho,\phi) &= Z_0^{\rho\rho} + P^{\rho\rho}(\rho,\phi) \\ Z_S^{\rho\phi}(\rho,\phi) &= -(Z_S^{\phi\rho}(\rho,\phi))^* = P^{\rho\phi}(\rho,\phi) \\ Z_S^{\phi\phi}(\rho,\phi) &= Z_0^{\phi\phi} - P^{\rho\rho}(\rho,\phi), \end{aligned} \tag{9}$$

where (ρ, ϕ) is the usual polar system of coordinates, and $P^{\rho\rho}$ and $P^{\rho\phi}$ describe the impedance modulation. The antennas are of circular shape and are fed with a coax feeder, modeled as an infinitesimal vertical dipole.

DIAMOND-SHAPED PATTERN IN THE UV-PLANE

Since the proposed synthesis method enables taking the desired radiation pattern directly as an input, a diamond-shaped pattern has been drawn in the *uv*-plane. From there, the desired current distribution is computed and is expanded

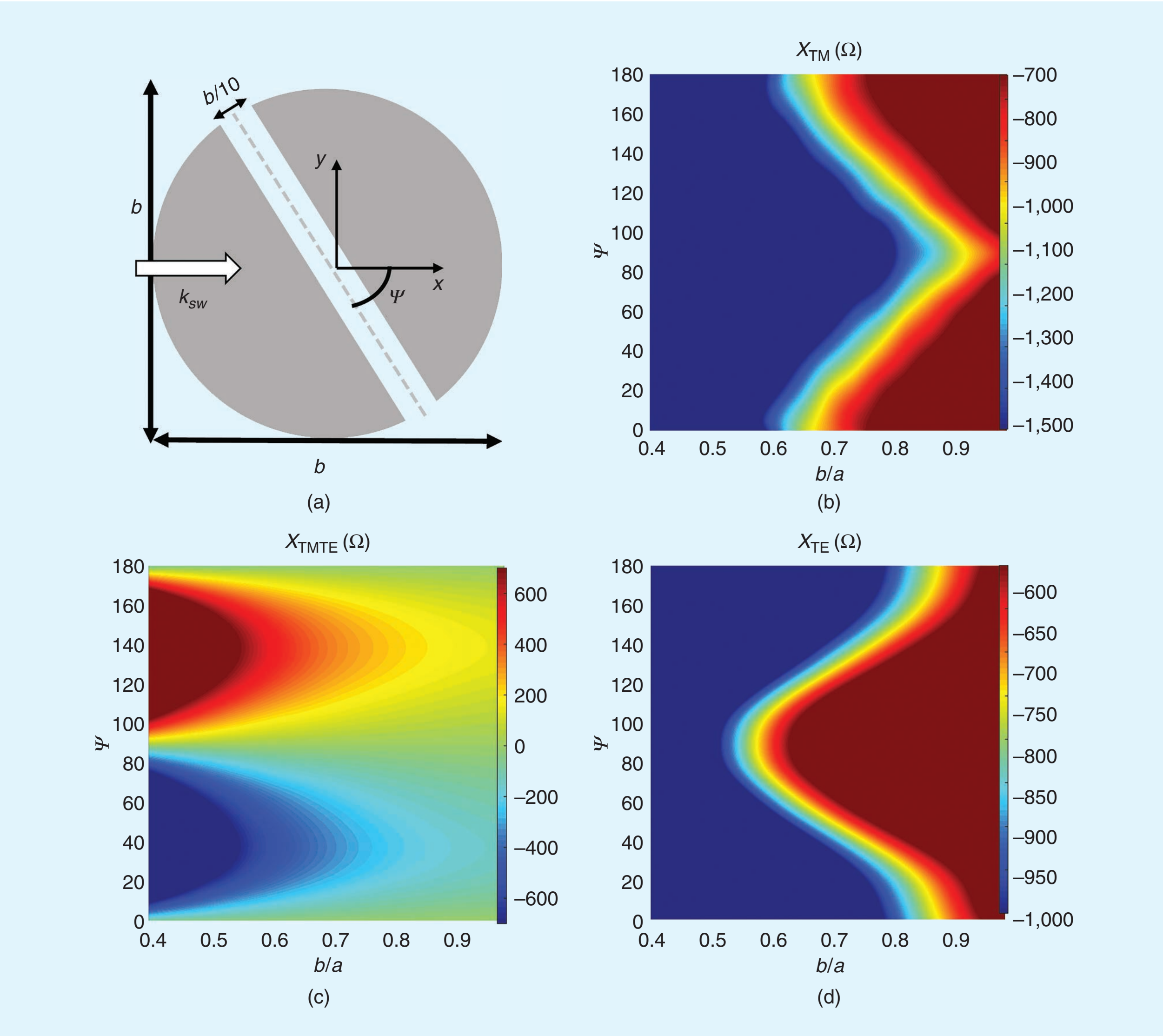

FIGURE 6. The coffee bean patches used for the IBC implementation: the (a) geometry as well as the (b) *TM*, (c) *TMTE*, and (d) *TE* reactance databases. a: the unit cell size; b: diameter of the coffee bean as shown in Figure 6(a); b/a: the ratio between b and a.

into the used set of basis functions—in our case, Fourier–Bessel basis functions [29], [30]. This expansion allows us to reconstruct the desired radiation pattern [see Figure 7(a)], taking into account the finite size of the antenna (here, a circular MTS of radius 4.5λ). The corresponding radiating current distribution on the antenna aperture is shown in Figure 7(b). The synthesized reactance modulation for a feeder placed at the center of the MTS ($\rho = 0$) is shown in Figure 8(a) and (b). Comparing the reactance modulation with the desired visible current, one can observe that the modulated portions of the antenna correspond to the radiating parts.

The directivity corresponding to the designed surface impedance (obtained with the code developed in [29]) is shown in the uv-plane in Figure 9(a) and (b). It can be seen that the diamond-shaped pattern is well generated. The conversion efficiency of this antenna is about 58%. This conversion efficiency cannot be significantly improved without deteriorating the shape of the beam. Increasing the conversion efficiency significantly requires the usage of a more complex feeder. This issue was recently treated in [6]. The synthesized surface impedance is now implemented by following the procedure described in the "From the Inverse Problem Solution to the Synthesis Algorithm" section. The obtained physical structure of the MTS is analyzed with the full-wave code presented in [35]. Figures 9(c) and (d) show the directivity comparisons in the planes $\phi = 0$ and $\phi = \pi/2$

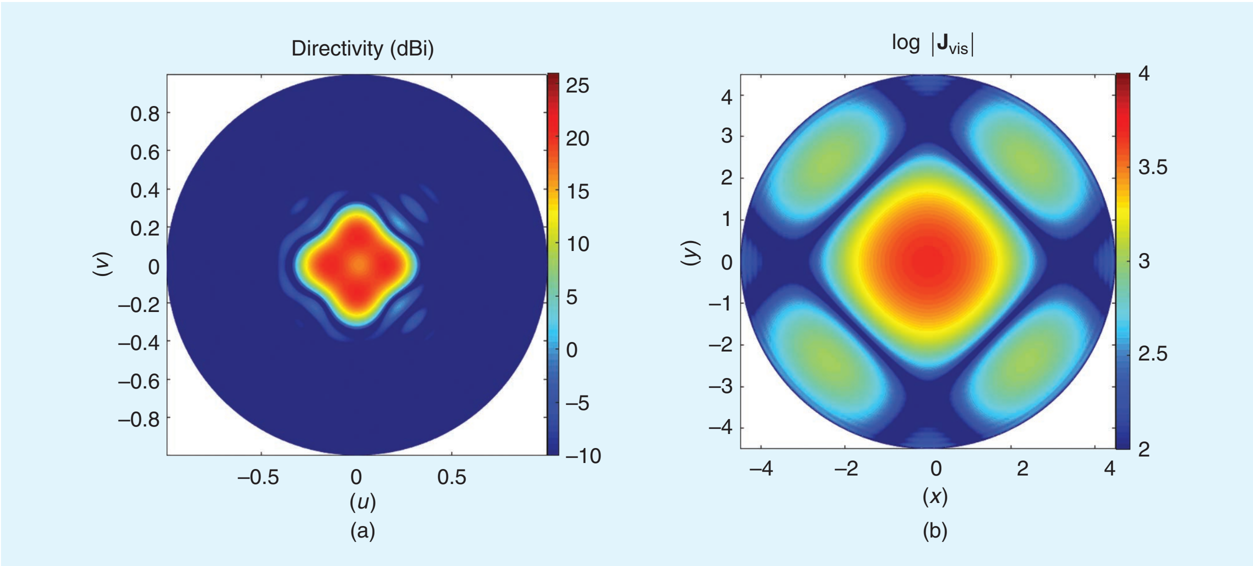

FIGURE 7. The desired diamond-shaped beam (a) in the uv-plane and (b) with the absolute value of the required visible (radiating) current distribution on a log scale.

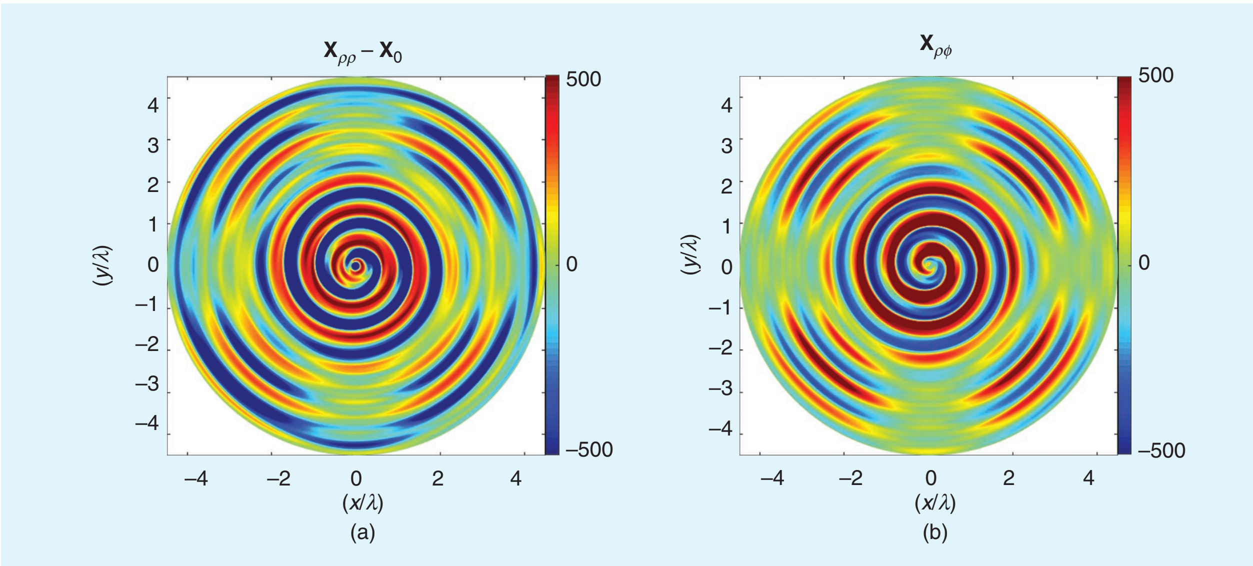

FIGURE 8. The diamond-shaped pattern for MTS design. (a) The $\rho\rho$ component of the reactance modulation. (b) The $\rho\phi$ component of the reactance modulation.

This article has been accepted for inclusion in a future issue of this journal. Content is final as presented, with the exception of pagination.

of the surface impedance and the MTS simulations. A very good agreement can be observed.

BUTTERFLY-SHAPED PATTERN IN THE UV-PLANE

To give an idea about the beam-shaping capability of the proposed method, we have designed a left-handed circularly polarized (LHCP), butterfly-shaped pattern in the uv-plane. The MTS is fed from the center, and its radius is fixed to 12λ. The synthesized MTS has been analyzed with the MOM method presented in [29]. Figure 10 shows the obtained results. As can be seen, the desired butterfly-shaped pattern is well obtained after synthesis.

LHCP CONICAL BEAM

This section deals with the realization of an MTS radiating an LHCP conical beam (at $\theta = 25^\circ$) with a uniform phase distribution along the azimuthal plane. The antenna radius has been fixed to 12λ, and the feeder is placed at the center of the MTS. The other parameters are the same as before. The designed sheet impedance modulation is illustrated in Figure 11(a) and (b). The reactance profile is azimuthally symmetric as required by the pattern symmetry. The corresponding antenna directivity in the plane $\phi = 0$ is compared with the desired one in Figure 11(c).

The surface impedance is then implemented with coffee bean patches with unit cells of size $\lambda/10$. The realized antenna is shown in Figure 12. The measured normalized directivity at three frequencies (23.7, 23.85, and 24 GHz) is shown in Figure 13. It is observed that the normalized directivity is better at 23.7 GHz, with a very low cross-polarization level (28 dB lower than the co-polarization level). This shift in the frequency of operation may be explained by the fabrication tolerance. However, higher sidelobe level are experimentally

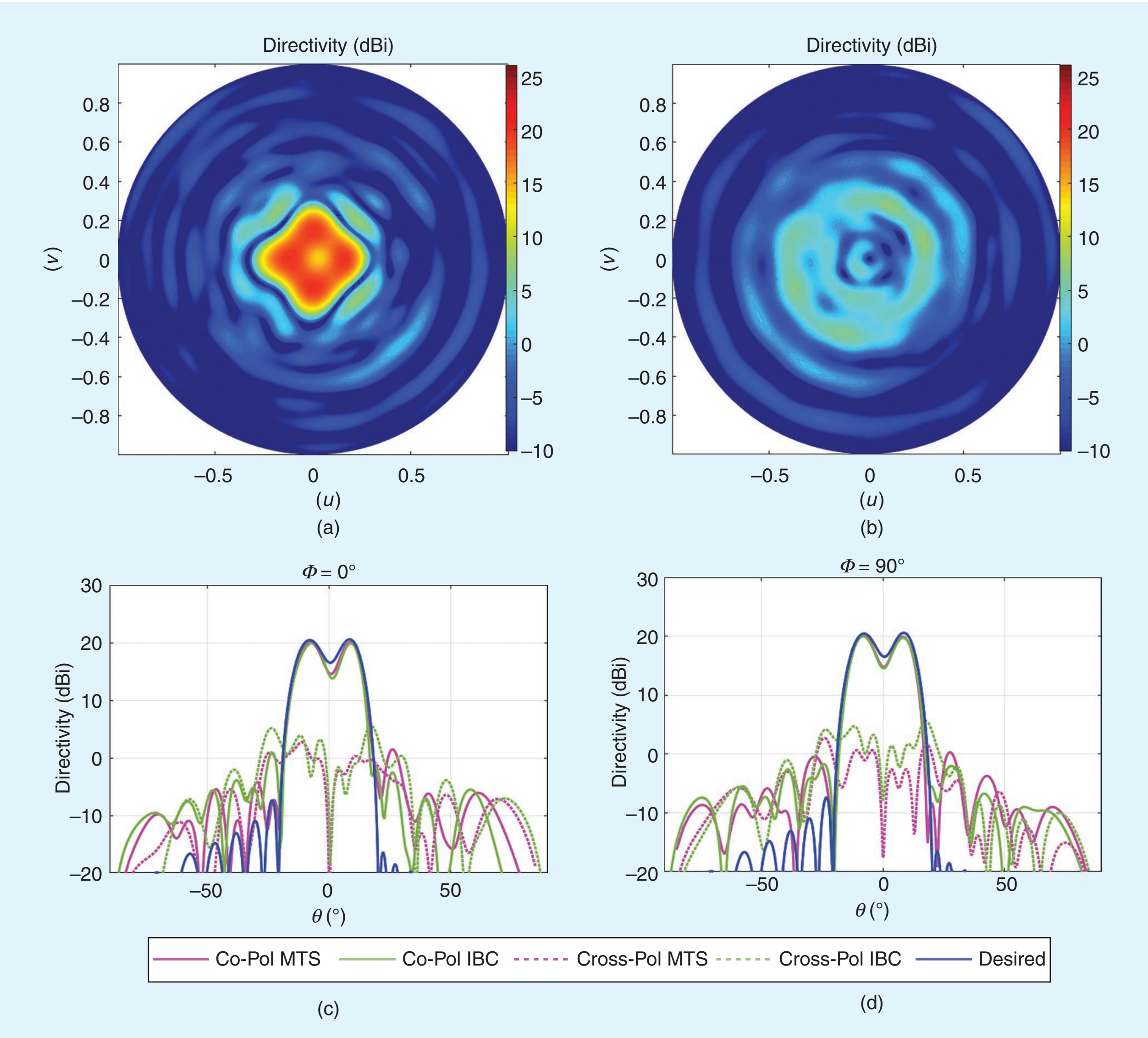

FIGURE 9. The diamond-shaped pattern for MTS design. (a) The copolarization (Co-pol) directivity in the uv-plane. (b) The cross-polarization (Cross-pol) directivity in the uv-plane. (c) The directivity cut in the plane $\phi = 0$. (d) The directivity cut in the plane $\phi = 90^\circ$.

observed near the broadside direction. This is, most probably, due to the error introduced during the surface impedance implementation process. Indeed, due to fabrication constraints, we were forced to limit the maximum diameter of the coffee bean patch to $0.91a$. This constraint introduces distortions on the surface impedance, limits the implemented modulation depth, and significantly impacts the sidelobe level near the broadside direction.

To support this assertion, we have considered the limitations due to fabrication constraints at the surface impedance level, and we numerically analyzed the effectively implemented surface impedance. The directivity result is shown in Figure 14. As can be seen, the sidelobe level has increased near the broadside with respect to the pattern obtained with the synthesized impedance. Unlike the diamond-shaped pattern case, the physical MTS structure of this antenna has not been analyzed due to its very large size. The numerical prediction of the measured sidelobe level at the broadside requires the full-wave simulation of the physical structure of the MTS.

Meshing this antenna aperture with classical basis functions would require the use of several million basis functions. In the future, full-wave analysis codes should be developed to address the simulation of larger MTS antennas so as to be able to check the accuracy of the implementation step before resorting to experimental verification. This experimental validation illustrates the capability of the proposed integral equation method to automatically generate complex radiation patterns.

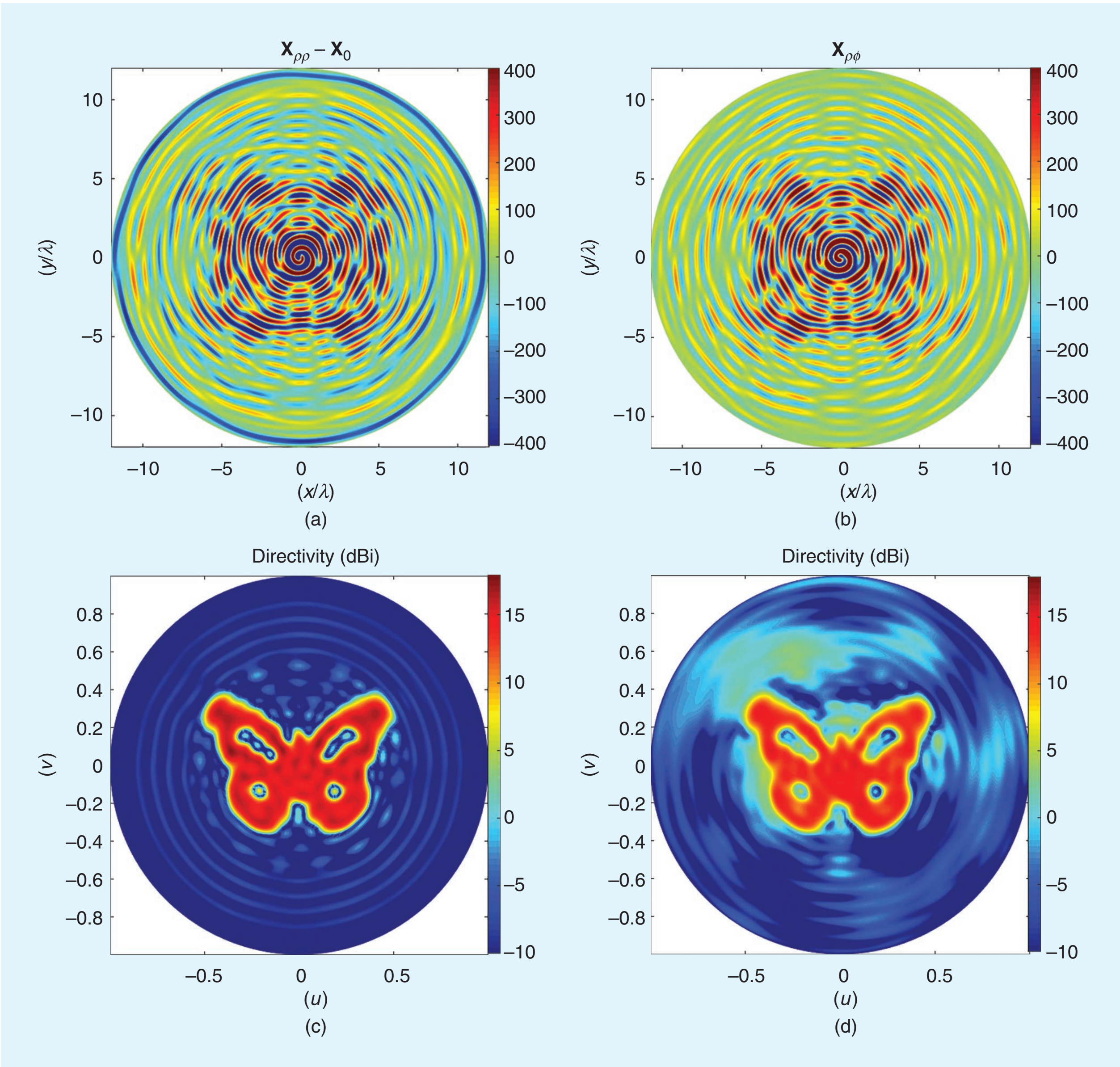

FIGURE 10. The butterfly-shaped pattern for MTS design. (a) The $\rho\rho$ component of the reactance modulation. (b) The $\rho\phi$ component of the reactance modulation. (c) The desired directivity in the uv-plane. (d) The obtained directivity after MTS synthesis.

PHASE CONTROL OF THE RADIATION PATTERN: A CONICAL BEAM WITH ORBITAL ANGULAR MOMENTUM

In the "LHCP Conical Beam" section, the MTS was designed to radiate a conical beam with a uniform phase distribution along azimuth ϕ. Although some authors have addressed the phase optimization issue [36], our proposed method aims at generating the pattern, including a prescribed phase distribution. To demonstrate the capability of the method to control

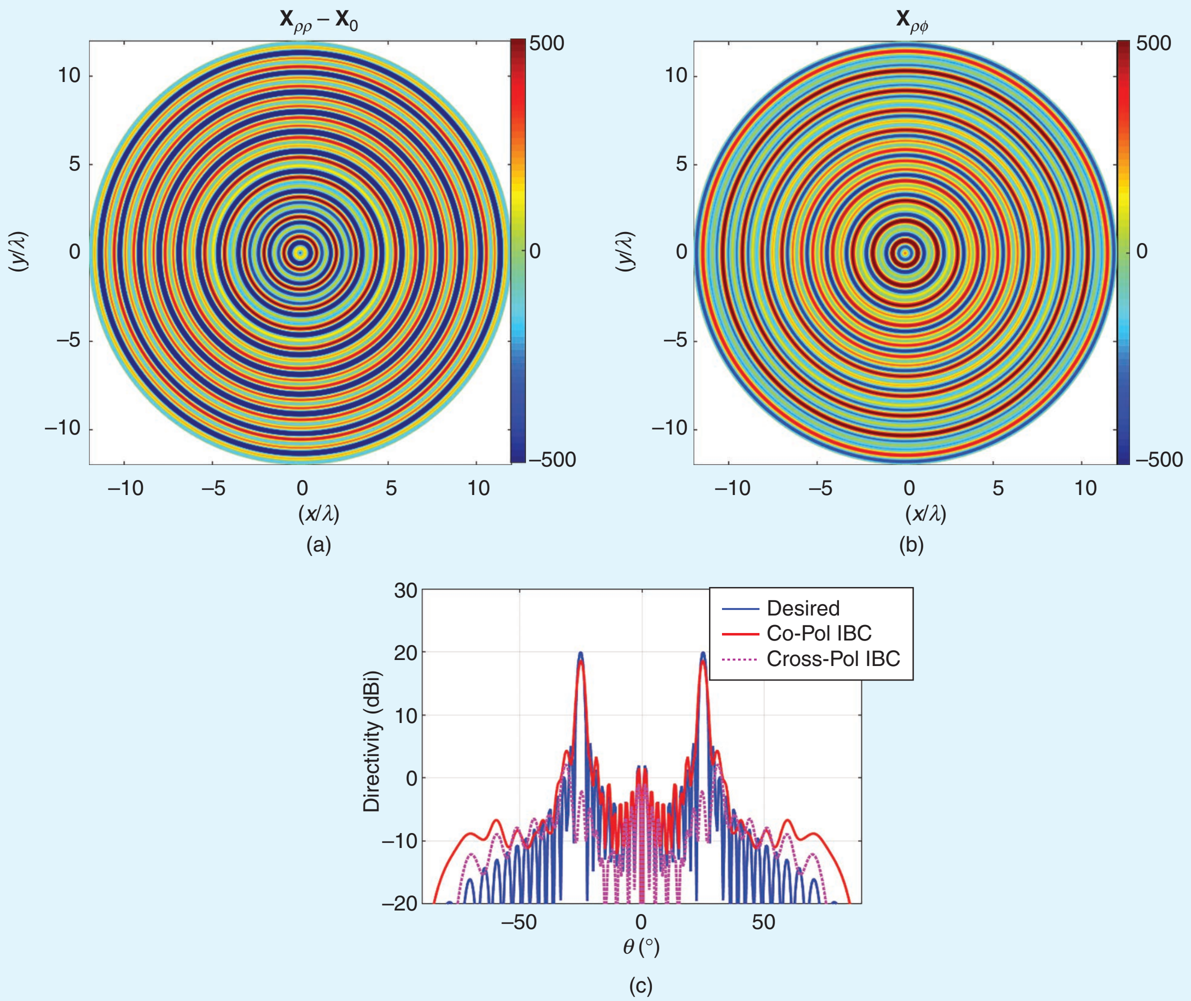

FIGURE 11. A circularly polarized conical beam MTS antenna. (a) The $\rho\rho$ component of the reactance modulation. (b) The $\rho\phi$ component of the reactance modulation. (c) The directivity cut in the plane $\phi = 0$ after IBC synthesis.

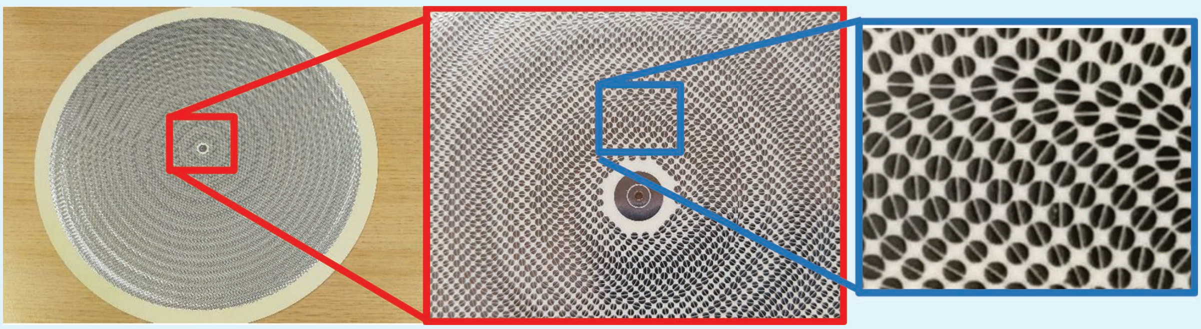

FIGURE 12. An MTS antenna radiating a circularly polarized conical beam.

the phase distribution, the MTS is now designed to radiate the same conical beam as in the "LHCP Conical Beam" section but with a linear phase evolution along the azimuth. The prescribed pattern at $\theta = 25^\circ$ is $F_\theta = \sin 3\phi + j\cos 3\phi$, and $F_\phi = jF_\theta$. For $\theta \neq 25^\circ$, $F_\theta = F_\phi = 0$. That means that the pattern carries out an orbital angular momentum (OAM) in the radiating direction.

Figure 15 shows the design results. As can be seen, we obtained approximately the same performance (in amplitude and polarization purity) as for the uniform phase case. However, here, the phase linearly evolves along the azimuth [Figure 15(d)]. This also indicates the remaining degrees of freedom regarding the phase pattern selection. However, in the cases treated so far, the choice of the phase distribution did not improve the performance significantly. We showed, in [37], that multiple OAM beams can be generated with the same MTS platform. One should note that OAM multiplexing is limited to the near field [38]. The phase control capability of the method was also used in [24] for beam-scanning purposes.

MULTIFUNCTIONAL MTS PLATFORM

Here, we design an MTS able to generate the same conical beam as in the "LHCP Conical Beam" section when the MTS is fed at $(x = 2\lambda, y = 0)$ and a pencil beam pointing at $(\theta = 30^\circ, \ \phi = 0^\circ)$ when the MTS is fed at $(x = -2\lambda, y = 0)$. Figure 16(a) and (b) shows the designed reactance modulation. Figure 16(c) and (d) provides the pattern corresponding to each beam using the MOM code described in [29]. As expected, given the limited number of degrees of freedom on the MTS, the two patterns are slightly spoiled. The obtained maximum directivity of the conical beam is now 15.5 dBi, which is lower than the one obtained with a single feeder (18.5 dBi). Note that, by following a similar procedure, the beams can also be designed at different frequencies (multiband) [25]. Those results illustrate the capability of the proposed method to produce multifunctional apertures.

CONCLUSIONS

This article provides numerical and experimental validation of an MTS antenna synthesis method based on the surface integral equation approach. The MTS designs provided here are of circular shape because entire-domain basis functions defined on the circular domain are used to drastically reduce the number of unknowns and synthesis computational time (fewer than 30 min for the examples provided). The algorithm has been extended to elliptical apertures in [7]. For arbitrarily shaped MTSs, local basis functions should be used at the expense of larger memory and computation time usage. Indeed, as for the analysis problems with MOM, this synthesis method can cope with local basis functions (e.g., rooftop basis functions). In that case, the required computational power seems affordable on present-day desktop computers.

As recently shown in [6], for a certain class of shaped beams, an array feeder may be preferred to the single monopole feeder to improve the conversion efficiency of the antenna. In this sense, arrays and MTS technologies should be combined to

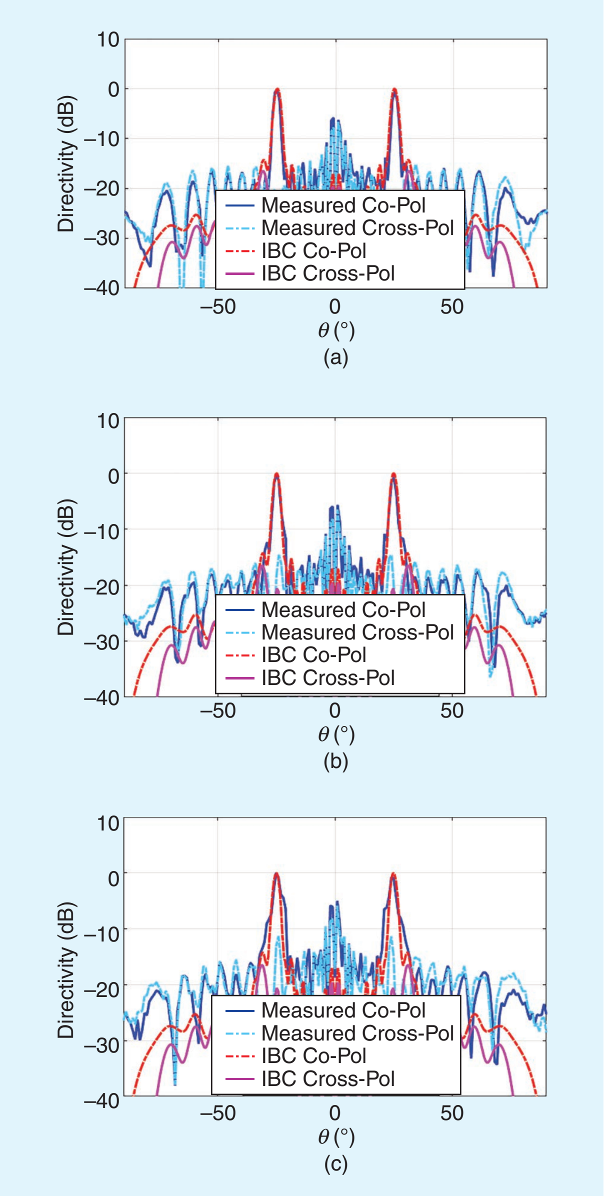

FIGURE 13. A comparison between the measurement results at different frequencies and the IBC simulation: (a) 23.7, (b) 23.85, and (c) 24 GHz.

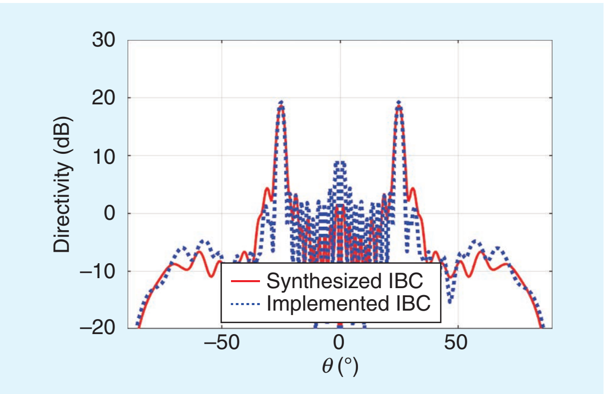

FIGURE 14. The effect of the IBC implementation inaccuracy. The inaccuracy mainly comes from fabrication limitations.

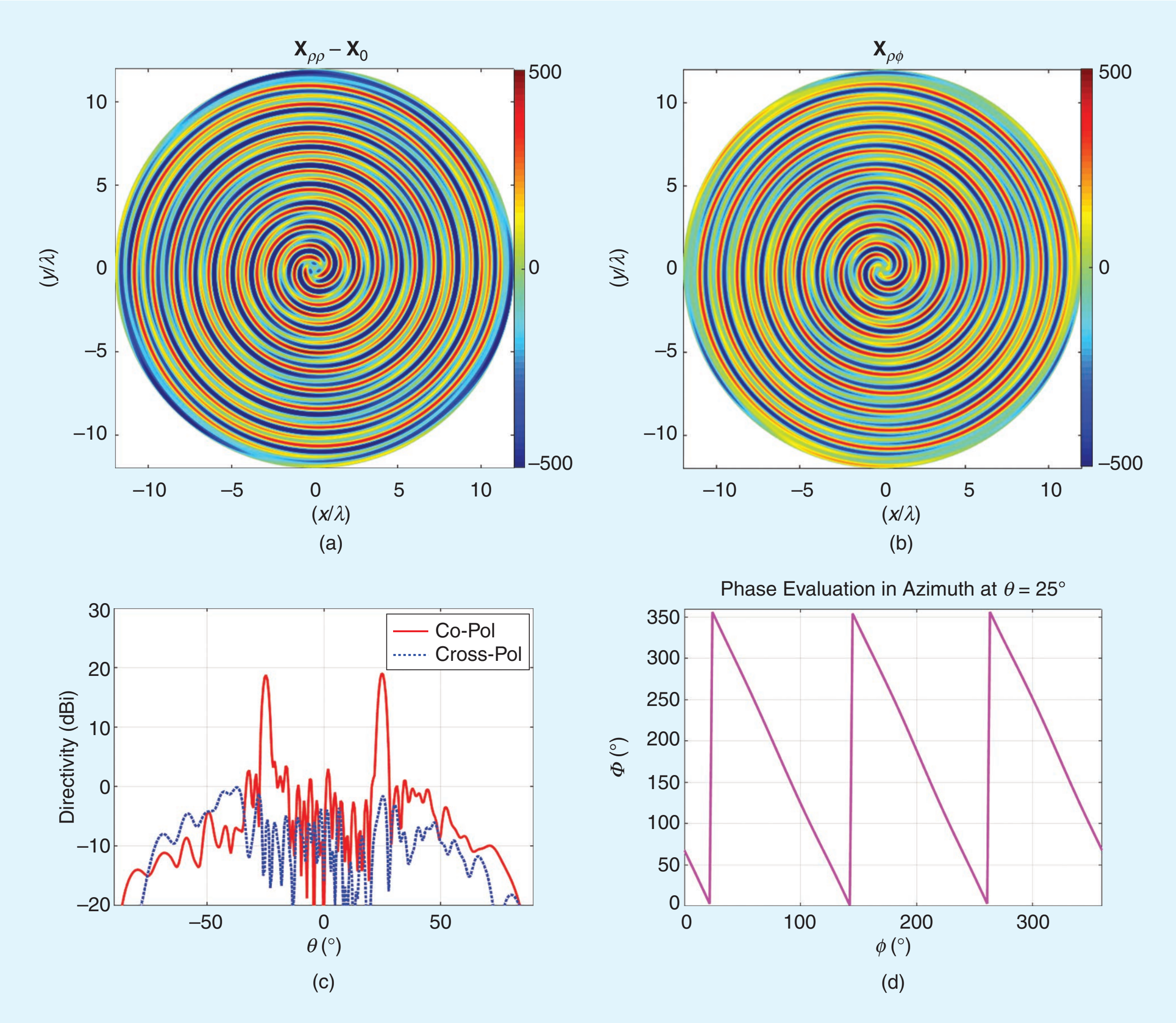

FIGURE 15. A conical beam with linear phase evolution in the azimuth. (a) The $\rho\rho$ component of the reactance modulation. (b) The $\rho\phi$ component of the reactance modulation. (c) The directivity cut in the plane $\phi = 0$. (d) The phase distribution in the cone $\theta = 25^{\circ}$.

achieve an efficient performance for shaped-beam, low-profile, and cheap antennas. As initiated in [24], array feeding may also contribute to scanning capabilities with a strongly reduced number of active channels. In that case, the phase distribution of the beam should be well controlled.

Progress in computational EM is required to monitor the implementation of the surface impedance in terms of patterned surfaces. Finally, advances in manufacturing techniques would also be useful to achieve satisfactory realization tolerance.

ACKNOWLEDGMENT

This research has been supported by the Belgian Fonds National de la Recherche Scientifique. Chargé de Recherche program. The authors would like to thank the antenna lab of the Institute of High Frequency Technology, Aachen University, for carrying out the measurement of the antenna shown in Figure 12.

AUTHOR INFORMATION

Modeste Bodehou (modeste.bodehou@uclouvain.be) is an FNRS postdoctoral researcher at Université Catholique de Louvain, Louvain-la-Neuve, 1348, Belgium. His research interests include computational electromagnetics, antenna arrays, and metasurfaces. He is a Member of IEEE.

Khaldoun Al Khalifeh (khaldoun.alkhalifeh@uclouvain.be) is a postdoctoral researcher at Université Catholique de Louvain, Louvain-la-Neuve, 1348, Belgium. His research interests include multiband antenna array design and analysis, ground-penetrating radar, and space applications. He is a Member of IEEE.

Shambhu Nath Jha (shambhu-nath.jha@be.thalesgroup.com) is an electromagnetics specialist at Thales Belgium, Tubize, 1480, Belgium. His research interests include electromagnetics and metasurfaces for various applications. He is a Senior Member of IEEE.

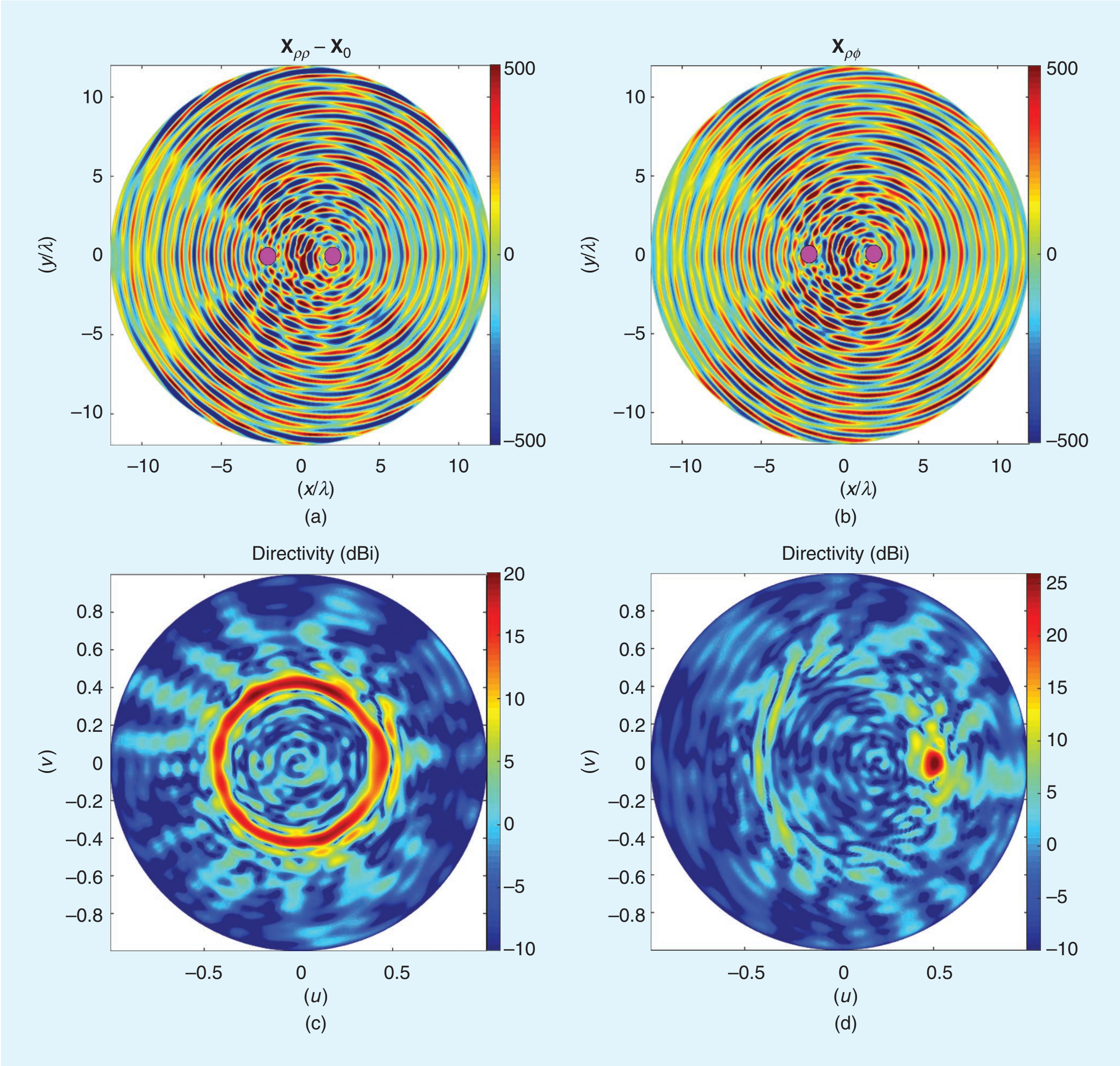

FIGURE 16. A multifunctional MTS antenna. (a) The $\rho\rho$ component of the reactance modulation. (b) The $\rho\phi$ component of the reactance modulation. (c) The directivity in the *uv*-plane when the first feed is activated. (d) The directivity in the *uv*-plane when the second feed is activated. The red dots in (a) and (b) represent the feed positions.

Christophe Craeye (christophe.craeye@uclouvain.be) is a professor at Université Catholique de Louvain, ICTEAM Institute, Louvain-la-Neuve, 1348, Belgium. His research interests include antenna arrays, metamaterials, and numerical methods for array analysis. He is a Senior Member of IEEE.

REFERENCES

[1] A. G. Toshev, "Synthesized shaped beam flat array antenna for digital beamforming radar applications, utilizing printed technology," in *Proc. IEEE Int. Conf. Microw. Antennas Commun. Electron. Syst.*, 2017, pp. 1–4, doi: 10.1109/COMCAS.2017.8244737.

[2] S. Moon, S. Yun, I. Yom, and H. L. Lee, "Phased array shaped-beam satellite antenna with boosted-beam control," *IEEE Trans. Antennas Propag.*, vol. 67, no. 12, pp. 7633–7636, Dec. 2019, doi: 10.1109/TAP.2019.2930129.

[3] H. A. Kayani, Q. Gueuning, N. Goreux, D. Vanhoenacker-Janvier, C. Oestges, and C. Craeye, "Reconfigurable cellular base station antenna consisting of parasitic radiators," *IEEE Trans. Ind. Electron.*, vol. 67, no. 8, pp. 7083–7093, Aug. 2020, doi: 10.1109/TIE.2019.2935991.

[4] M. Faenzi *et al.*, "Metasurface antennas: New models, applications and realizations," *Scientific Rep.*, vol. 9, p. 10,178, Jul. 2019, doi: 10.1038/s41598-019-46522-z.

[5] M. Bodehou, C. Craeye, E. Martini, and I. Huynen, "A quasi-direct method for the surface impedance design of modulated metasurface antennas," *IEEE Trans. Antennas Propag.*, vol. 67, no. 1, pp. 24–36, 2019, doi: 10.1109/TAP.2018.2874762.

[6] M. Bodehou and C. Craeye, "Array surface-wave launcher for the efficient generation of shaped beam and multibeam with metasurfaces," *IEEE Trans. Antennas Propag.*, vol. 69, no. 12, pp. 8860–8865, Dec. 2021.

[7] M. Bodehou, C. Craeye, and I. Huynen, "Electric field integral equation-based synthesis of elliptical-domain metasurface antennas," *IEEE Trans. Antennas Propag.*, vol. 67, no. 2, pp. 1270–1274, Feb. 2019, doi: 10.1109/TAP.2018.2880122.

[8] O. Quevedo-Teruel *et al.*, "Roadmap on metasurfaces," *J. Opt.*, vol. 21, no. 7, p. 073002, 2019, doi: 10.1088/2040-8986/ab161d.

[9] C. L. Holloway and E. F. Kuester, "Generalized sheet transition conditions for a metascreen – A fishnet metasurface," *IEEE Antennas Propag. Mag.*, vol. 66, no. 5, pp. 2414–2427, Feb. 2018, doi: 10.1109/TAP.2018.2809620.
[10] N. Yu *et al*., "Flat optics: Controlling wavefronts with optical antenna metasurfaces," *IEEE J. Sel. Topics Quantum Electron.*, vol. 19, no. 3, p. 4,700,423, May 2013, doi: 10.1109/JSTQE.2013.2241399.
[11] C. Pfeiffer and A. Grbic, "Metamaterial Huygens' surfaces: Tailoring wave fronts with reflectionless sheets," *Phys. Rev. Lett.*, vol. 110, no. 19, p. 197,401, May 2013, doi: 10.1103/PhysRevLett.110.197401.
[12] N. M. Estakhri and A. Alu, "Wave-front transformation with gradient metasurfaces," *Phys. Rev. X*, vol. 6, p. 041008, Oct. 2016.
[13] A. Epstein and G. V. Eleftheriades, "Synthesis of passive lossless metasurfaces using auxiliary fields for reflectionless beam splitting and perfect reflection," *Phys. Rev. Lett.*, vol. 117, no. 25, p. 256,103, 2016, doi: 10.1103/PhysRevLett.117.256103.
[14] L. Liang and S. V. Hum, "Design of a UWB reflectarray as an impedance surface using Bessel filters," *IEEE Trans. Antennas Propag.*, vol. 64, no. 10, pp. 4242–4255, Oct. 2016, doi: 10.1109/TAP.2016.2594056.
[15] M. D. Renzo *et al.*, "Smart radio environments empowered by reconfigurable intelligent surfaces: How it works, state of research, and the road ahead," *IEEE J. Sel. Areas Commun.*, vol. 38, no. 11, pp. 2450–2525, 2020, doi: 10.1109/JSAC.2020.3007211.
[16] A. Oliner and A. Hessel, "Guided waves on sinusoidally-modulated reactance surfaces," *IRE Trans. Antennas Propag.*, vol. 7, no. 5, pp. 201–208, Dec. 1959, doi: 10.1109/TAP.1959.1144771.
[17] B. H. Fong, J. S. Colburn, J. J. Ottusch, J. L. Visher, and D. F. Sievenpiper, "Scalar and tensor holographic artificial impedance surfaces," *IEEE Trans. Antennas Propag.*, vol. 58, no. 10, pp. 3212–3221, Oct. 2010, doi: 10.1109/TAP.2010.2055812.
[18] A. M. Patel and A. Grbic, "A printed leaky-wave antenna based on a sinusoidally-modulated reactance surface," *IEEE Trans. Antennas Propag.*, vol. 59, no. 6, pp. 2087–2096, Jun. 2011, doi: 10.1109/TAP.2011.2143668.
[19] G. Minatti *et al.*, "Modulated metasurface antennas for space: Synthesis, analysis and realizations," *IEEE Trans. Antennas Propag.*, vol. 63, no. 4, pp. 1288–1300, Apr. 2015, doi: 10.1109/TAP.2014.2377718.
[20] G. Minatti, F. Caminita, E. Martini, M. Sabbadini, and S. Maci, "Synthesis of modulated-metasurface antennas with amplitude, phase, and polarization control," *IEEE Trans. Antennas Propag.*, vol. 64, no. 9, pp. 3907–3919, Sep. 2016, doi: 10.1109/TAP.2016.2589969.
[21] D. González-Ovejero, G. Minatti, G. Chattopadhyay, and S. Maci, "Multibeam by metasurface antennas," *IEEE Trans. Antennas Propag.*, vol. 65, no. 6, pp. 2923–2930, Jun. 2017, doi: 10.1109/TAP.2017.2670622.
[22] M. Faenzi, D. González-Ovejero, and S. Maci, "Wideband active region metasurface antennas," *IEEE Trans. Antennas Propag.*, vol. 68, no. 3, pp. 1261–1272, Mar. 2020, doi: 10.1109/TAP.2019.2940365.
[23] G. Minatti, F. Caminita, E. Martini, and S. Maci, "Flat optics for leaky-waves on modulated metasurfaces: Adiabatic Floquet-wave analysis," *IEEE Trans. Antennas Propag.*, vol. 64, no. 9, pp. 3896–3906, Sep. 2016, doi: 10.1109/TAP.2016.2590559.
[24] M. Bodehou, E. Martini, S. Maci, I. Huynen, and C. Craeye, "Multibeam and beam scanning with modulated metasurfaces," *IEEE Trans. Antennas Propag.*, vol. 68, no. 3, pp. 1273–1281, 2020, doi: 10.1109/TAP.2019.2944554.
[25] M. Bodehou, C. Craeye, and I. Huynen, "Multifrequency band synthesis of modulated metasurface antennas," *IEEE Antennas Wireless Propag. Lett.*, vol. 19, no. 1, pp. 134–138, 2020, doi: 10.1109/LAWP.2019.2955895.
[26] R. G. Harrington, *Field Computation by Moment Methods*. New York, NY, USA: Wiley, 1993.
[27] J. Budhu, A. Grbic, and E. Michielssen, "Design of multilayer, dualband metasurface reflectarrays," in *Proc. 14th Eur. Conf. Antennas Propag. (EuCAP)*, 2020, pp. 1–4, doi: 10.23919/EuCAP48036.2020.9135957.
[28] M. Bodehou, D. González-Ovejero, C. Craeye, S. Maci, I. Huynen, and E. Martini, "Power balance and efficiency of metasurface antennas," *Scientific Rep.*, vol. 10, p. 17,508, Oct. 2020, doi: 10.1038/s41598-020-74674-w.
[29] M. Bodehou, D. González-Ovejero, C. Craeye, and I. Huynen, "Method of moments simulation of modulated metasurface antennas with a set of orthogonal entire-domain basis functions," *IEEE Trans. Antennas Propag.*, vol. 67, no. 2, pp. 1119–1130, 2019, doi: 10.1109/TAP.2018.2880075.
[30] M. Bodehou, C. Craeye, H. Bui-Van, and I. Huynen, "Fourier-Bessel basis functions for the analysis of elliptical domain metasurface antennas," *IEEE Antennas Wireless Propag. Lett.*, vol. 17, no. 4, pp. 675–678, Apr. 2018, doi: 10.1109/LAWP.2018.2811620.
[31] M. Salucci, A. Gelmini, G. Oliveri, N. Anselmi, and A. Massa, "Synthesis of shaped beam reflectarrays with constrained geometry by exploiting nonradiating surface currents," *IEEE Trans. Antennas Propag.*, vol. 66, no. 11, pp. 5805–5817, 2018, doi: 10.1109/TAP.2018.2869036.
[32] G. Minatti, S. Maci, P. De Vita, A. Freni, and M. Sabbadini, "A circularly-polarized isoflux antenna based on anisotropic metasurface," *IEEE Trans. Antennas Propag.*, vol. 60, no. 11, pp. 4998–5009, Nov. 2012, doi: 10.1109/TAP.2012.2208614.
[33] N. Guerin, C. Craeye, and X. Dardenne, "Accelerated computation of the free space Green's function gradient of infinite phased arrays of dipoles," *IEEE Trans. Antennas Propag.*, vol. 57, no. 10, pp. 3430–3434, Oct. 2009, doi: 10.1109/TAP.2009.2028684.
[34] S. Maci and A. Cucini, "FSS-based EBG surfaces," in *Electromagnetic Metamaterials: Physics and Engineering Aspects*, R. Ziolkowski and N. Engheta, Eds. New York, NY, USA: Wiley, 2006, pp. 351–376.
[35] S. Hubert, S. N. Jha, and C. Craeye, "Analysis of large nonregular printed scatterers using the Contour-FFT," *IEEE Trans. Antennas Propag.*, vol. 66, no. 11, pp. 6115–6127, Nov. 2018, doi: 10.1109/TAP.2018.2864314.
[36] S. Pearson and S. V. Hum, "Using augmented Lagrangian methods to design electromagnetic surfaces with far field constraints," in *Proc. IEEE Int. Symp. Antennas Propag. North Amer. Radio Sci. Meeting (AP-S/URSI)*, Jul. 2020, pp. 969–970, doi: 10.1109/IEEECONF35879.2020.9329978.
[37] M. Bodehou, C. Craeye, and I. Huynen, "Near-field shaping by leaky-wave metasurfaces: OAM and Bessel beams synthesis," in *Proc. 2019 Int. Conf. Electromagn. Adv. Appl.*, pp. 1210–1213, doi: 10.1109/ICEAA.2019.8879142.
[38] M. Tamagone, C. Craeye, and J. Perruisseau-Carrier, "Comment on encoding many channels on the same frequency through radio vorticity: First experimental test," *New J. Phys.*, vol. 14, no. 11, p. 118,001, Nov. 2012, doi: 10.1088/1367-2630/14/11/118001.